Progress in Additive Manufacturing (2023) 8:745–757
https://doi.org/10.1007/s40964-023-00428-5

FULL RESEARCH ARTICLE

Forced-response characterization of PBF-LB/AlSi10Mg particle dampers with thin and flat cavities

Julius Westbeld[1] · **Fabio von Coburg**[1] · **Philipp Höfer**[1]

Received: 28 October 2022 / Accepted: 4 March 2023 / Published online: 27 March 2023

Abstract
Powder Bed Fusion (PBF) enables the production of complex geometries which offer the opportunity to manufacture lightweight, stiffness-optimised or integrally designed components. Although these properties are usually advantageous for the performance in many applications, they pose disadvantages under vibration as they lead to low damped components. These are prone to high vibration amplitudes which result in higher sound radiation and a reduced lifetime. Particle damping can counteract these disadvantages. By including cavities during the design process, unmelted powder remains inside the component after its production. This powder dissipates energy under vibration by inelastic impacts and friction in particle-particle or particle-wall-interactions, increasing the damping characteristics of the component. In this work, additively manufactured AlSi10Mg specimens with cavities are investigated with respect to their damping characteristics by experimental modal analysis. The focus of the investigation is on thin and flat cavities that can be easily integrated into components without adapting the external geometry. The damping characteristics in dependence on excitation amplitude and mode are quantified. The extent to which settling effects of the powder during shaking influence the damping is analysed. The vibration of the specimens is forced by an electrodynamic shaker and their response is measured contactlessly via Scanning Laser Doppler Vibrometry (SLDV). A damping effect of up to 564% depending on the mode, excitation amplitude and specimen can be achieved. In addition, a significant settling effect of the powder which hampers the damping effect is identified by CT scans and modal analysis.

Keywords Additive manufacturing (AM) · Particle damping · Thin cavities · Laser powder bed fusion (PBF-LB) · AlSi10Mg · Functional integration

1 Introduction

Over the last decade, the use of additive manufacturing (AM) has gained significance in structural industrial applications due to several benefits AM and especially Laser Powder Bed Fusion (PBF-LB) provides compared to conventional manufacturing processes [1]. Relevant for the present study are its abilities to manufacture integrally designed components on one hand and lightweight structures on the other hand. Integral components are designed to have as few parts as possible, where each part carries multiple functions [2]. This is beneficial from an industrial manufacturing perspective but also from a performance perspective as it increases strength and decreases weight [3]. In general, lightweight design offers the opportunities to realize higher accelerations, increase payload and reduce spent energy, which is especially advantageous in the aerospace, automotive and energy sector [4]. The often-desired high stiffness-per-weight-ratio can be achieved by topology optimization and its geometrically complex solutions are suitable for PBF-LB [5]. Several industrial applications show PBF-LB being used to manufacture lightweight, comparably stiff and integrally designed structural components [6–13]. However, these specific benefits become drawbacks under vibration as lightweight structures are more prone to vibration [14–16], stiff structures have a reduced component damping [17] and the lack of friction in joints decreases the damping characteristics of integrally designed components [18]. This leads to a reduced lifespan of the components and a higher sound radiation [19].

✉ Julius Westbeld
julius.westbeld@unibw.de

[1] Institute of Lightweight Engineering, University of the Bundeswehr Munich, Werner-Heisenberg-Weg 39, 85577 Neubiberg, Germany

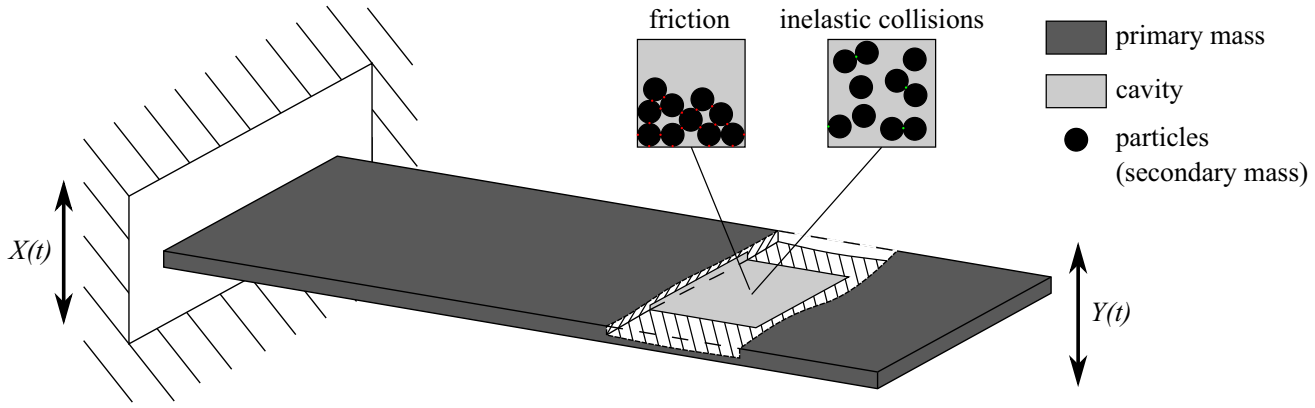

Fig. 1 Schematic diagram of an additively manufactured particle damper showing system excitation *X(t)* and system response *Y(t)* and depicting the two effect mechanisms of energy dissipation; based on [28]

One method to counteract these susceptibilities is the use of particle damping. In this passive damping system, the component consists of a solid (primary) mass and a versatile (secondary) particle mass. This secondary mass can be attached to the primary mass as an outside container or can be inserted into the primary mass [20–22]. Under vibration, the secondary mass dissipates energy by inelastic collisions or friction at particle-particle or particle-wall interfaces, see Fig. 1 [23]. PBF-LB offers the opportunity to inherently include particle damping by designing cavities inside of the component in which unfused powder remains after manufacturing. Following the "Complexity for free" concept [24], Ehlers et al. [25] have coined the expression "Damping for free" as this technique neither increases component mass nor manufacturing cost compared to the fully fused reference component. However, for now, modelling of conventional as well as AM particle dampers is not reliable as the damping characteristics are highly non-linear and dependent on multiple design parameters like the cavity size, cavity position, excitation amplitude and frequency [26, 27]. Nevertheless, some research regarding AM particle dampers has been carried out:

Ehlers et al. [25, 28] characterized additively manufactured particle dampers of different materials depending on excitation force and frequency for different cavity sizes. One dimension of their slender specimens was up to two orders of magnitude larger than the other two dimensions with a cavity located throughout the centre of the whole specimen. The most significant increase of damping by a factor of 28 for tool steel 1.2709 and a factor of 18 for aluminium alloy AlSi10Mg was observed. Heat treatment of Ti6Al4V specimens prevented any significant damping effect. Schmitz et al. [29–31] investigated beam-shaped aluminium specimens with inner cavities of 5 – 9 mm diameter and laser beam melted walls out of AISI 316L stainless steel with ~ 20 – 60% cavity volume and different internal ribs. At most, the damping was increased by a factor of 225 at the third mode. Künneke and Zimmer [32] studied a more general approach and investigated the damping characteristics of AISI 316L stainless steel particle dampers independently of the stiffness of the vibrating mass using a power measurement technique. In a previous study, Künneke and Zimmer [33] showed the ability to reduce sound radiation by additively manufactured particle damping in an electromagnetic spring-applied brake.

Although these studies show great potential for additively manufactured particle dampers, the integrability into aerodynamic designs like integrally bladed rotors (IBRs) in turbines or other two-dimensional structures can be better achieved by thin and flat cavities. When positioned at the neutral axis, these would also only have a small impact on structural integrity. Particle damping with thin and flat cavities was analysed by Scott-Emuakpor et al. [34–38] with specimens manufactured of Inconel 718 and AISI 316L stainless steel. Their first hypothesis of a densely packed interior pocket and thereby minimized impact behaviour as dissipation mechanism [37] did not hold as CT scans revealed empty spaces in the pocket [38]. Even for low cavity volumes of 1 – 4% compared to the previously mentioned studies, the component damping was increased by a factor of up to 10.

In the present study, specimens with one thin and flat cavity out of AlSi10Mg powder are analysed, which is a less dense and typically coarser powder compared to the material in previously mentioned studies. The overall specimen behaviour is measured via Scanning Laser Doppler Vibrometry (SLDV) under several different excitation amplitudes to characterise the non-linear particle damping. In addition, settling effects of the powder are depicted which are attributed to the experimental setup and significantly decrease the effectiveness of the particle damping.

Table 1 Frequency parameters $\beta_n l$ for the first five bending modes $n = 1 \ldots 5$ [40]

n	1	2	3	4	5
$\beta_n l$	1.8751	4.6941	7.8548	10.996	14.1372

2 Methods

2.1 Specimen design

Two kinds of specimens were designed. The "solid" specimens are fully fused and serve as a baseline for modal parameters. The "cavity" specimens have the same outer geometry as the solid specimens and differ only by an internal cavity. The specimens are of cuboidal geometry with a length of $l_{tot} = 120$ mm in accordance with the capabilities of the PBF-LB machine employed and to obtain low and, therefore, well measurable resonance frequencies. To investigate thin and flat cavities, the other two dimensions of the specimen are chosen to be $w = 24$ mm and $h = 2$ mm. The cavity is positioned in the neutral axis of the specimen and has a thickness of $h_{cav} = 0.67$ mm. To keep the aim of thin and flat cavities in mind, the other two dimensions are chosen to $w_{cav} = l_{cav} = 15$ mm. As the specimens are clamped at one side with a clamping length of $l_{BC} = 20$ mm, the remaining $l = l_{tot} - l_{BC} = 100$ mm can oscillate. The positioning of the cavity along the length of the specimen is chosen, so that it would not overlap with a node point in the first three bending modes, as previous studies have shown a larger damping effect for particle dampers being placed in areas of larger displacement for conventional [39] as well as additive particle dampers [35].

The bending mode shapes Φ_n for the bending mode n are calculated according to classical beam theory for undamped cantilever beams

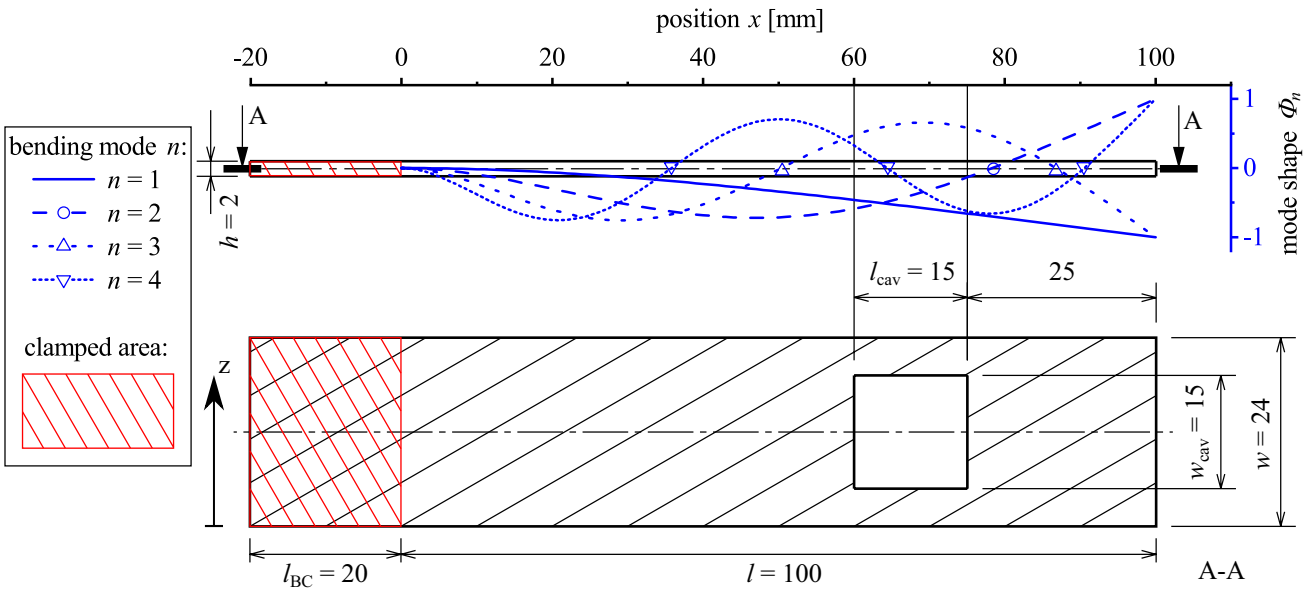

Fig. 2 Dimensions of the cavity specimen in mm with the clamped area (red) and the printing direction (z) as well as the bending mode shapes $\Phi_n(x)$ for $n = 1 \ldots 4$ with the respective node points according to classical beam theory

Table 2 Process parameters for specimen production on SLM 125

	Volume	Up-skin	Down-skin
scan strategy	Stripes (10 mm)	Stripes (1 mm)	
hatch distance [mm]	0.13	0.1	
power [W]	350	350	300
scanning speed [mm/s]	1650	830	1600
number of borders	1		0
border power [W]	220		–
border scanning speed [mm/s]	730		–
layer thickness [µm]	30		
atmosphere	Argon		

Table 3 Powder properties of material in the present study compared to similar studies with thin and flat cavities

	AlSi10Mg (data sheets)	AlSi10Mg (measured)	AISI 316L	Inconel 718
Mass density ρ [g/cm^3]	~2.67 [41]	–	~7.9 [44]	~8.2 [45]
Mean particle size D_{mean} [µm]	45.2 – 49.5	45.0 [46]	~30 [35]	~27 [35]

$$\Phi_n(x) = \sinh(\beta_n x) - \sin(\beta_n x) - \frac{\sinh(\beta_n l) + \sin(\beta_n l)}{\cosh(\beta_n l) + \cos(\beta_n l)}\left(\cosh(\beta_n x) - \cos(\beta_n x)\right) \tag{1}$$

with the position x along the length l and the frequency parameter β_n [40]. The frequency equation

$$1 + \cosh(\beta_n l)\cos(\beta_n l) = 0 \tag{2}$$

shows that the frequency parameter β_n can take any of a countable set of values, see Table 1. This leads to the first four bending mode shapes according to Fig. 2. The positioning of the outwards boundary of the cavity is chosen to be 25 mm from the free end as this would lead to no overlap between cavity and a node point in the first three bending modes. Nevertheless, a node point in the fourth bending mode and the cavity coincide.

2.2 Laser beam powder bed fusion

The specimens are manufactured out of AlSi10Mg on an SLM 125 PBF-LB machine with process parameters which can be found in Table 2.

The properties of the AlSi10Mg powder in Table 3 are obtained by supplied data sheets from the powder manufacturer as well as previous work on powder characterisation by a Bettersizer S3 Plus for the used powder batch. It shows the significantly lower density and courser particle size compared to the powder in similar studies. The Young's modulus $E = 74000$MPa for this set of parameters and the Poisson's ratio $\nu = 0.35$ are taken from literature [41, 42]. The coordinate system according to DIN standard [43] is used.

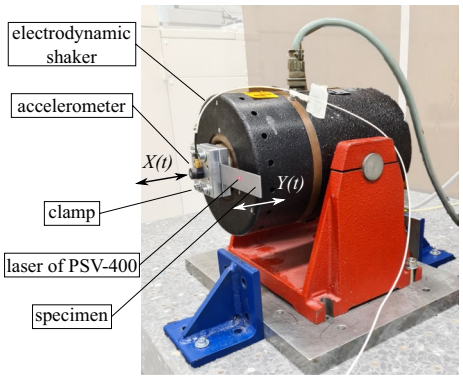

Fig. 4 Experimental setup of the electrodynamic shaker with the specimen in the clamp, the accelerometer to measure the system excitation *X(t)* and the laser point from the PSV-400 to measure the system response *Y(t)*

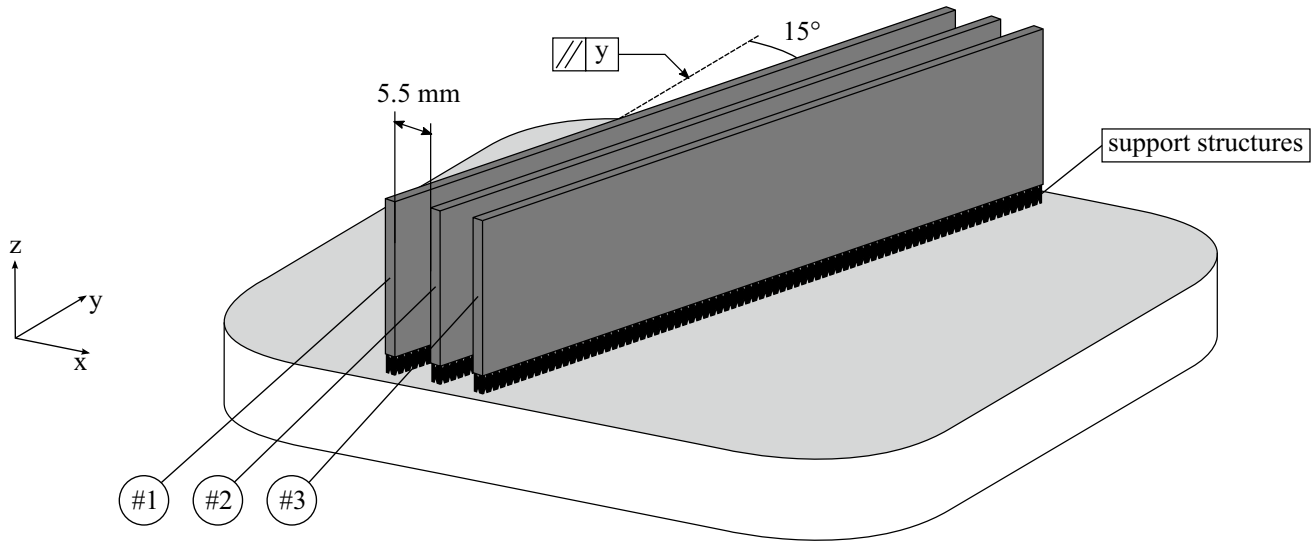

Fig. 3 Specimens #1 - #3 on an SLM 125 build platform depicting their position and orientation, the machine coordinate system and support structures (black)

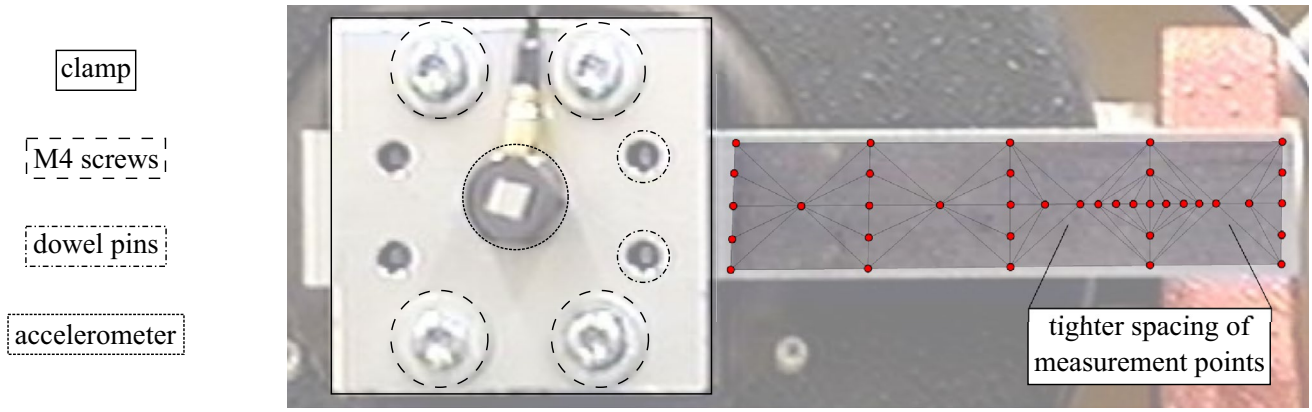

Fig. 5 Specimen in the clamp as seen from the PSV-400 with the 37 scanning points (red) distributed over the specimen; the M4 screws, dowel pins, the accelerometer and the tighter positioned scanning points around the cavity are highlighted

Table 4 Calculated natural bending frequencies f_n^* for the bending modes $n = 1 \ldots 5$ according to classical beam theory

n	1	2	3	4	5
f_n^* [Hz]	170.1	1065.9	2984.6	5849.1	9668.2

Three cavity specimens (labelled #1 – #3) and two solid specimens (labelled #4 & #5) are manufactured. They are positioned on the build platform with the longest dimension in y-direction and the second longest dimension in z-direction, see Fig. 2. This results in an overhang of 0.67 mm in the cavity which is manufacturable without support structures [47]. The specimens are rotated by 15° around the z-axis to avoid recoater crashes and separated by 5.5 mm, see Fig. 3. Due to manufacturing constraints, the specimens have to be manufactured on two different build jobs. It is chosen that the cavity specimens are manufactured on the same build job to ensure their comparability. After the manufacturing processes, the specimens are sawn from the building platforms and cleaned in an ultrasonic bath. The remaining support structures to the building platform are milled off. No subsequent heat treatment nor other mechanical finishing or sandblasting is carried out.

2.3 Experimental setup

The specimens are sequentially clamped on an electrodynamic shaker (RMS SW 121) to analyse their modal parameters. Four M4 screws hold the specimen in place and are tightened with a defined torque of 6 Nm. Two dowel pins in the clamp prevent the slipping of the specimen. The system excitation in the time domain *X(t)* is measured with an accelerometer (Kistler 8630B50) on the clamp and the system response in the time domain *Y(t)* is measured by SLDV (Polytec PSV-400), see Fig. 4. This experimental setup is based on [48].

To examine the overall specimen behaviour, 37 points on a specimen are measured sequentially, see Fig. 5. The measurement points around the cavity are positioned more tightly to identify a possible special specimen behaviour at this location. The natural bending frequencies f_n^* are estimated according to classical beam theory for undamped cantilever beams, compare [48, 49].

$$f_n^* = \frac{(\beta_n l)^2 h}{2\pi l^2} \sqrt{\frac{E}{12\rho}} \tag{3}$$

The results can be seen in Table 4. They are taken as an estimation to define the measured frequency range. The applicability to the cavity specimens with their increased damping characteristics as well as their density and elasticity discontinuity around the cavity is evaluated during the experiments.

The specimens are excited with periodic chirps in the range of $f = 50$–6000 Hz with a frequency resolution of 500 mHz. This excites the first four bending resonance frequencies $n = 1 \ldots 4$, see Table 4. The excitation acceleration *X(f)* is kept constant over all frequencies within one measurement for a better comparability between the modes. Every measurement is repeated $k_a^{\#} \geq 4$ times to form one measurement batch per specimen # and excitation amplitude a. By this, the dependency of modal parameters on shaking duration is examined. *X(f)* is then varied after one measurement batch from 100 mm/s^2, 200 mm/s^2, 400 mm/s^2 up to 800 mm/s^2 per frequency bin to identify the non-linear damping characteristics of particle damping mentioned previously. The system response is transferred to the frequency domain *Y(f)*, averaged over all 37 measurement points and the frequency response function FRF*(f)* is calculated, compare [50].

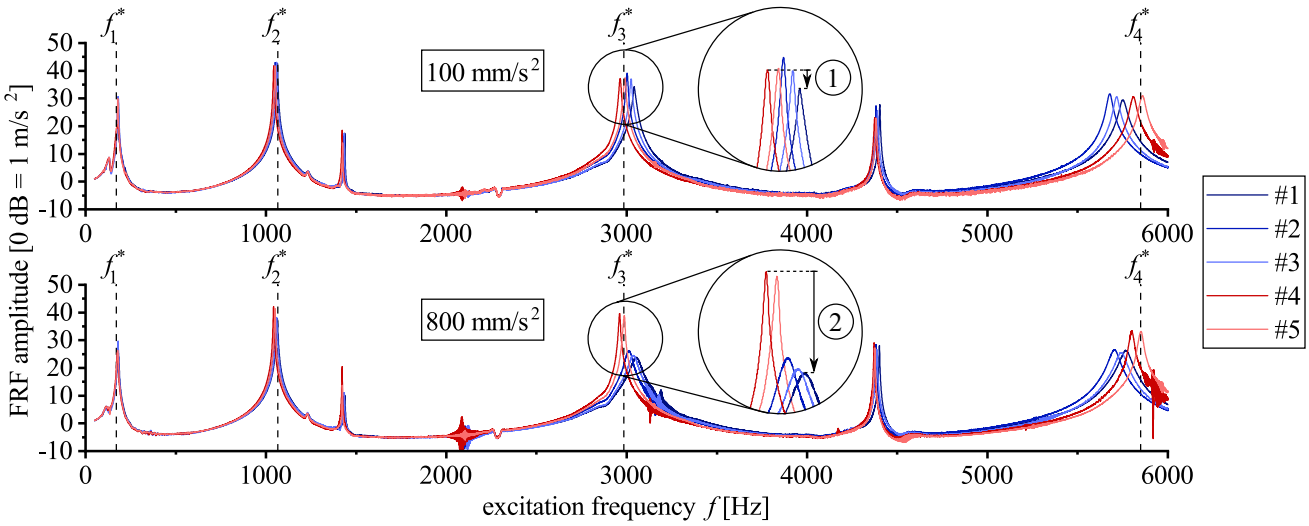

Fig. 6 FRFs of all specimens for the excitation amplitudes 100 mm/s^2 (top) and 800 mm/s^2 (bottom) as well as the calculated natural bending frequencies f_n^*; the higher damping at 800 mm/s^2 (2) compared to 100 mm/s^2 (1) is highlighted exemplarily for the third bending mode

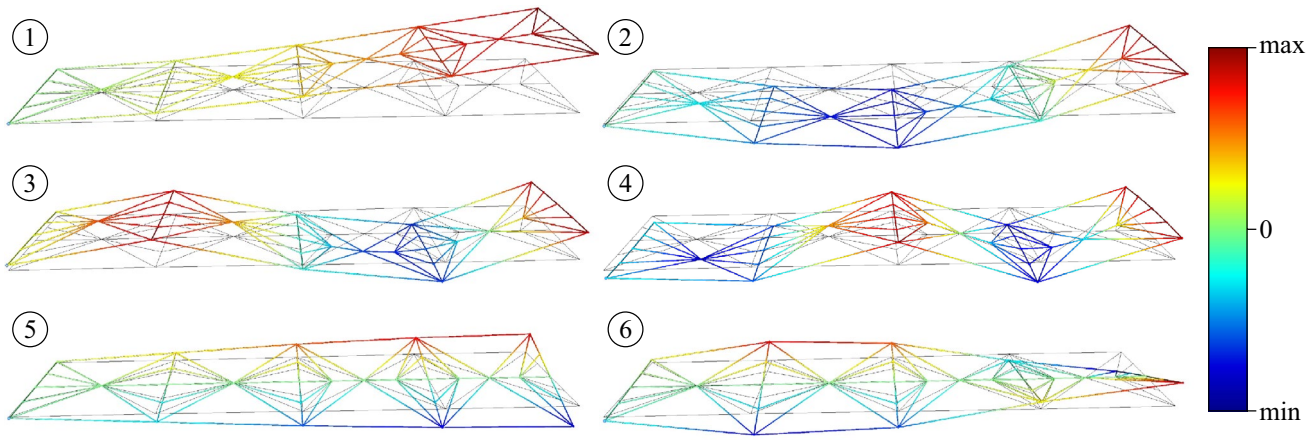

Fig. 7 Qualitative comparison between the displacement of the first six mode shapes; (1) - (4) show the first four bending modes and (5) & (6) show the first two torsional modes

$$\mathrm{FRF}(f) = \frac{Y(f)}{X(f)} \tag{4}$$

Each FRF is evaluated with the half-power bandwidth method to calculate the resonance frequencies f_n and loss factors η_n [48].

2.4 Computed tomography

The distribution of particles inside the cavity before and after the modal analysis is examined by computed tomography (CT) scans. A Bruker microCT SkyScan 1173 with an image pixel size between 10 – 15 µm is utilised and several measures during the reconstruction of the 3D-data are taken to achieve calibrated and, therefore, comparable images. The orientation of the specimens during CT scanning is in an upright position, meaning that the longest dimension of the specimen is parallel to the direction of gravity and the specimen is rotated around this axis during the scan. Therefore, the orientation of the specimen is different during CT scanning and modal analysis.

3 Results

3.1 Modal analysis

The FRFs show six distinct peaks, see Fig. 6, which correspond to the first four bending modes, as estimated in Table 4. The other two distinct peaks at about 1400 Hz

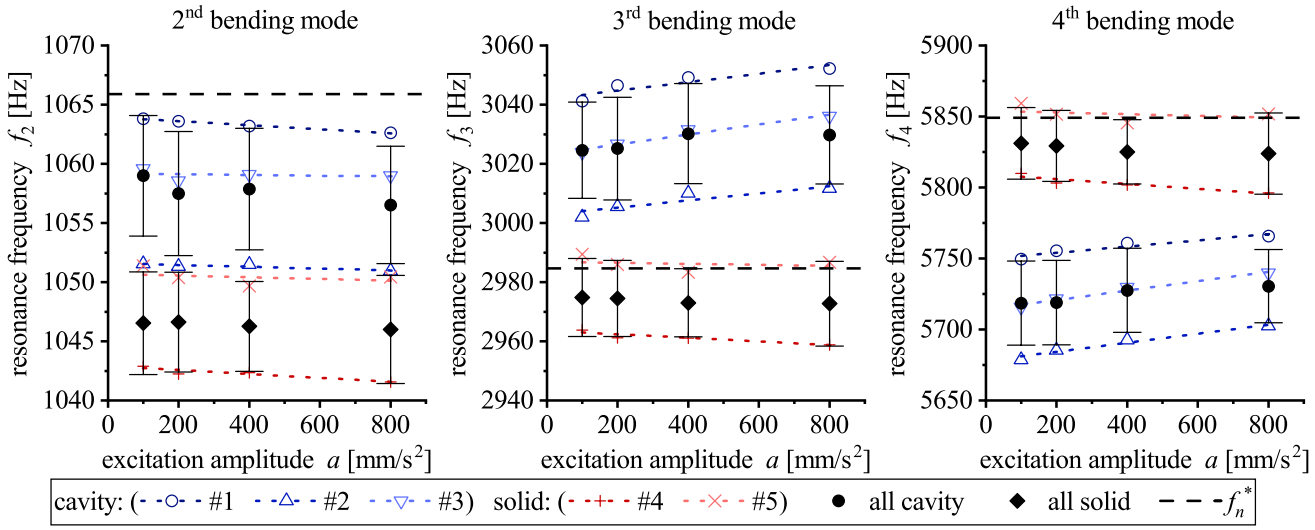

Fig. 8 Measured resonance frequencies f_n of all specimens and calculated natural bending frequencies f_n^* for the second-to-fourth bending modes $n = 2 \ldots 4$ over the excitation amplitude a; the standard deviation $s_{f,\mathrm{kind}}$ for all specimens of same kind (black) are depicted

Table 5 Relative difference of the loss factor at 800 mm/s^2 compared to the loss factors at 100 mm/s^2 with 100 mm/s^2 as a baseline for each considered mode

n	#1 (cavity) (%)	#2 (cavity) (%)	#3 (cavity) (%)	#4 (solid) (%)	#5 (solid) (%)
2	70.5	58.4	73.8	− 15.1	3.2
3	279.3	336.5	401.1	− 27.2	− 14.3
4	61.3	89.1	92.4	− 27.0	− 24.5

and 4400 Hz visible in Fig. 6 depict the first two torsional modes. The corresponding mode shapes can be seen in Fig. 7. Looking at Fig. 6, it is clearly visible that at 800 mm/s^2 the damping is much higher for the cavity specimens than for the solid specimens. At 100 mm/s^2 the difference in damping is less prominent. A closer look on

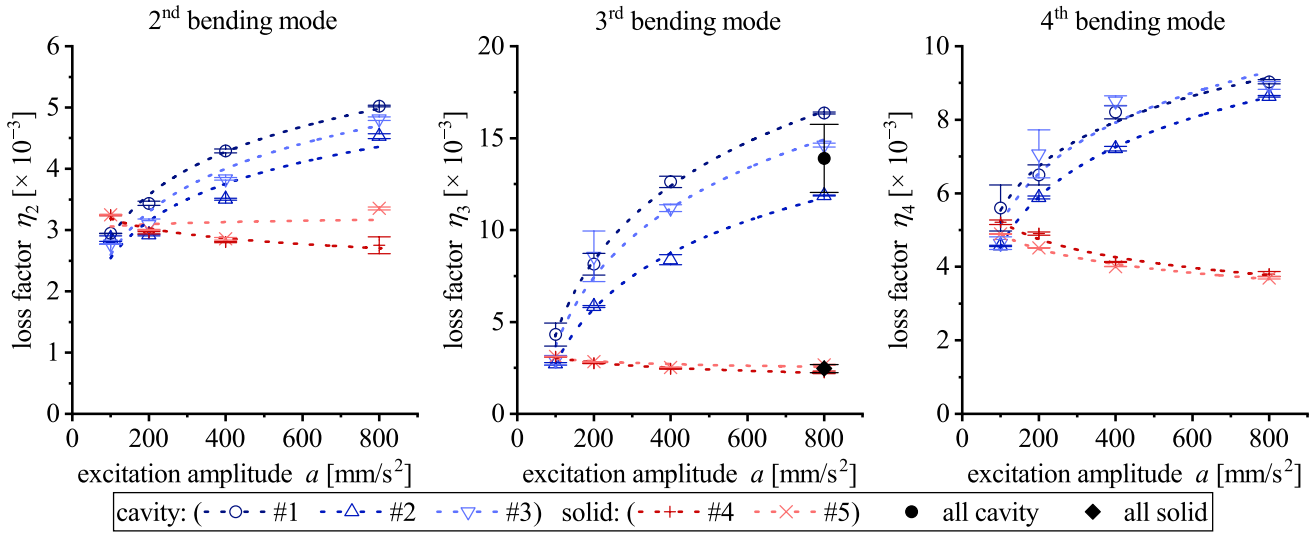

Fig. 9 Loss factor η_n of all specimens for the second-to-fourth bending modes $n = 2 \ldots 4$ over the excitation amplitude a; the standard deviation $s_{\eta,\mathrm{mb}}$ in each measurement batch (color) and the standard deviation $s_{\eta,\mathrm{kind}}$ for all specimens of same kind for the third bending mode at 800 mm/s^2 (black) are depicted exemplarily; the data follows logarithmic trend curves

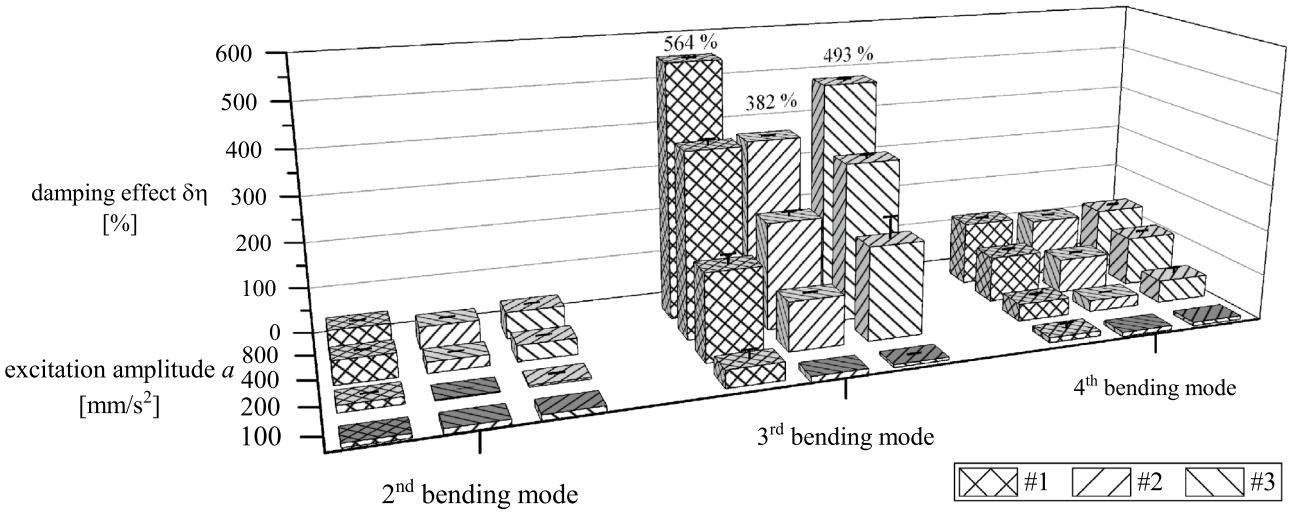

Fig. 10 Damping effect $\delta\eta$ for all cavity specimens for all considered modes at all examined excitation amplitudes a; the highest measured damping effect for each specimen is quantified

the dependency of modal parameters on excitation amplitudes is taken.

The resonance frequencies over the excitation amplitudes for all five specimens as well as the calculated natural frequencies from Table 4 can be seen in Fig. 8. The data from the first bending mode is disregarded as it is often done in similar studies [37], because large tip deflections lead to parasitic friction in the clamped components which influences component damping [28].

Three different characteristics can be highlighted: (1) the standard deviation $s_{f,\mathrm{mb}}$ in each measurement batch, (2) the difference of the resonance frequencies over the excitation amplitude and (3) the standard deviation $s_{f,\mathrm{kind}}$ for all specimens of same kind at the same excitation amplitude. The results show a very low $s_{f,\mathrm{mb}}$ for all measurement batches with a maximum of 0.036% in relation to the respective mean resonance frequency. This is so small that $s_{f,\mathrm{mb}}$ is not depicted in Fig. 8 due to visibility reasons, which indicates no relevant effect of shaking duration on the resonance frequencies. The resonance frequencies of each solid specimen decrease over excitation amplitude, see Fig. 8. The resonance frequencies of each cavity specimen also decrease over excitation amplitude for the second bending mode but increase for the third and fourth bending mode. Nevertheless, Fig. 8 shows as well that this effect is not significant when focussing at all specimens of same kind due to the large standard deviation $s_{f,\mathrm{kind}}$.

The loss factor η over the excitation amplitudes for all five specimens and all considered bending modes is shown in Fig. 9. Similar to the assessment of the resonance frequencies, three characteristics of the loss factor η for every mode are highlighted: (1) The standard deviation $s_{\eta,\mathrm{mb}}$ in each measurement batch is with a maximum of 16% in relation to the respective mean loss factor significantly higher compared to $s_{f,\mathrm{mb}}$, see Fig. 9. The distribution of loss factor in dependence of shaking duration is, therefore, checked in the following paragraph. (2) The difference of the loss factor over the excitation amplitude with 100 mm/s^2 as a baseline is calculated for each specimen and mode, see Table 5. It shows first that the loss factors of the cavity specimens vary a lot more compared to the solid specimens. Second, the change in loss factor for the cavity specimens is by a factor of 4–6 higher in the third bending mode compared to the other modes and thirdly it can be seen that there is a slight decrease in loss factor for the solid specimens. (3) The standard deviation $s_{\eta,\mathrm{kind}}$ for all specimens of same kind at the same excitation amplitude show a much wider spread between cavity specimens than between solid specimens, see Fig. 9. Therefore, the mean of loss factor of the $k_a^{\#1/\#2/\#3}$ measurements for each cavity specimen at a specific excitation amplitude a for a specific mode n

$$\mathrm{mean}_{\eta}^{\#1/\#2/\#3} = \frac{1}{k_a^{\#1/\#2/\#3}} \sum_{j=1}^{k_a^{\#1/\#2/\#3}} \eta_{\mathrm{mode},a,j}^{\#1/\#2/\#3} \tag{5}$$

is put into relation to the mean of loss factor of all $k_a^{\#4/\#5}$ measurements for both solid specimens

$$\mathrm{mean}_{\eta}^{\#\mathrm{solid}} = \frac{1}{k_a^{\#4} + k_a^{\#5}} \left(\sum_{j=1}^{k_a^{\#4}} \eta_{\mathrm{mode},a,j}^{\#4} + \sum_{j=1}^{k_a^{\#5}} \eta_{\mathrm{mode},a,j}^{\#5} \right) \tag{6}$$

to calculate the damping effect $\delta\eta$ for each cavity specimen

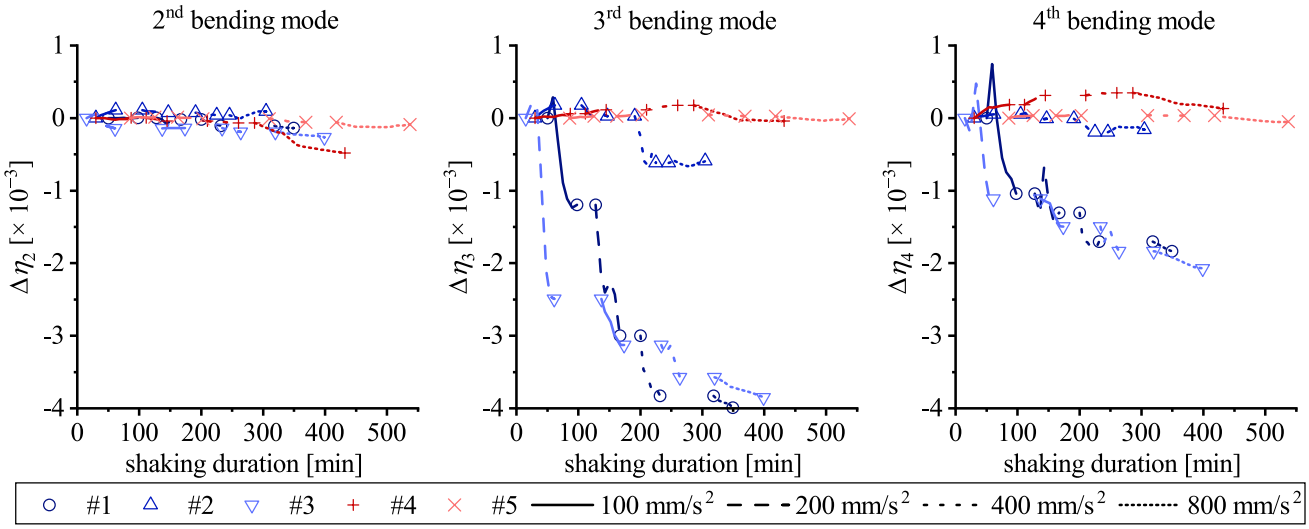

Fig. 11 Difference in loss factor $\Delta\eta_n$ over shaking duration for all specimens at all considered modes

$$\delta\eta_{\mathrm{mode},a}^{\#1/\#2/\#3} = \frac{\mathrm{mean}_{\eta}^{\#1/\#2/\#3}}{\mathrm{mean}_{\eta}^{\#\mathrm{solid}}} - 1 \tag{7}$$

which expresses the difference of the loss factor of a specific cavity specimen in comparison with the solid specimens for the same mode and at the same amplitude.

The damping effect for all cavity specimens for all considered modes can be found in Fig. 10. The bending modes show little to no damping effect for the lower excitation amplitudes. In contrast, the damping effect increases for higher excitation amplitudes. A positive damping effect can be seen for all bending modes but most prominently for the third bending mode. The damping of the torsional modes was also analysed but no significant damping effect was measured.

Because $s_{\eta,\mathrm{mb}}$ shows a significant variance in the damping characteristics per measurement batch, a closer look at each measurement is taken and a decrease in damping over time is identified. To quantify this decrease in loss factor, the difference in loss factor between adjacent measurements within one batch $\Delta\eta_n$ is calculated, sequentially accumulated, and plotted against shaking duration of the respective specimen, see Fig. 11. As several batches are measured consecutively without removing the specimen from the shaker, their $\Delta\eta_n$ is offset by the final accumulated difference in damping of the prior batch to visualize the total accumulated difference in loss factor over the entire shaking duration. This shows a low and random variation in loss factor for the solid specimens in all bending modes, but a decrease of loss factor over shaking duration for the cavity specimens, particularly in the third and fourth bending mode. This is especially prominent for the specimens #1 and #3, which are also the ones with the significantly higher damping effect, see Fig. 10. The measurement sequence described in Sect. 2.3 was unintentionally altered for specimen #3 by switching the order of the 100 mm/s^2 and 200 mm/s^2 measurement batches. When comparing specimen #3 with specimen #1, this does not seem to have a significant effect. However, comparing the accumulated total difference in loss factor over shaking duration of specimens #1/#3 with specimen #2 another influence factor shows a bigger influence which is discussed later in this study.

3.2 Computed tomography

To understand the decrease in loss factor and the particle distribution inside the cavity better, the CT scans of specimens before and after shaking is analysed. As mentioned before, the specimen orientations during CT scanning and modal analysis differ from each other, see Fig. 12. Before shaking, the particles fill up the whole cavity and are evenly distributed. Neither pockets of empty space nor regions with significantly higher packing density are formed. After shaking, a gradient of packing density in the direction of gravity during shaking $\vec{g}_{\mathrm{shake}}$ can be identified as the radiodensity in the cavity after shaking is higher at the bottom and lower at the top as shown in the graph in Fig. 12. In addition, small pockets of empty space at the cavity side against the direction of gravity during shaking can be seen. No gradient of packing density in the direction of gravity during CT scanning $\vec{g}_{\mathrm{CT}}$ or formation of empty space at the cavity side against this direction can be identified.

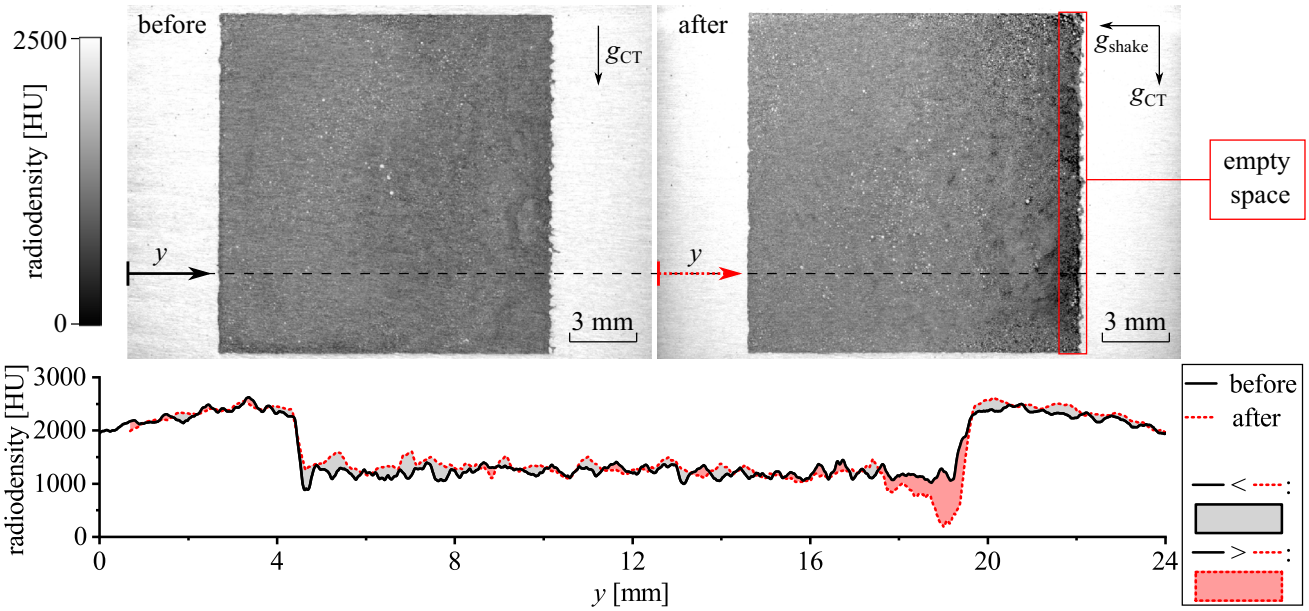

Fig. 12 CT scans of specimen #1 before shaking (left) and after shaking (right); the graph in the lower section shows the radiodensity of both scans at the same vertical position along the coordinate y which is indicated in the scans overhead; the directions of gravity during shaking g_{shake} and during CT scanning g_{CT} are given; the empty space in the cavity after shaking is highlighted

4 Discussion

The results in the present study show a considerable damping effect, which is mainly dependent on three parameters: (1) the specific cavity specimen, (2) the mode and (3) the excitation amplitude. The dependency of the damping effect on the specimen (1) can be identified in all examined modes: The damping performance of specimen #2 is always (and sometimes substantially) below the specimens #1 and #3 at comparable modes and excitations. The difference between the specimens of same design is probably based on differences in the manufacturing process or a potentially different handling of the specimens between manufacturing and experiment. The experimental setup is excluded as root cause as the specimens are remounted on the shaker and similar results as in the present study are achieved. The influence of the mode (2) on the damping effect could have two different explanations: The position of the cavity regarding the mode shape as well as the resonance frequency at the mode could be the root cause for the significantly higher damping in the third bending mode. A combination of both explanations is also conceivable and could be investigated by changing the length of the specimen and the position of the cavity in subsequent studies. Scott-Emuakpor et al. [35] proposed a multi-factor model to predict the damping performance, which would need to be validated for specimens out of AlSi10Mg. The dependency on the mode is also linked to the dependency on the specimen as the standard deviation $s_{\eta,\mathrm{kind}}$ for all cavity specimens at the third bending mode is significantly higher compared to the other bending modes, see Fig. 9. The nonlinearity of particle damping, and therefore, the dependency on the excitation amplitude (3) is already mentioned in Sect. 1 of this article as well as in literature [26, 27]. Subjected to a higher excitation amplitude, the particles in the cavity move more thereby dissipating more energy via the two effect mechanisms of particle damping depicted in Fig. 1. The well fit logarithmic trend curves for particle damping need to be verified with data for excitation amplitudes between the chosen amplitudes in the present study and beyond that, to ensure if the depicted trend persists. The damping effects measured by Scott-Emuakpor et al. [37] with similar specimen out of denser material were higher but in the same order of magnitude.

The decrease of resonance frequencies of the solid specimens, see Fig. 8, could be influenced by a slight opening of the clamp when the specimens move with larger amplitudes. This would elongate the swinging length according to Eq. (3) by 0.1% which corresponds here to 0.1 mm. The resonance frequencies of the cavity specimens on the other hand increase with excitation amplitude for the third and fourth bending mode, which are the modes with the highest damping effect at 800 mm/s^2, see Fig. 10. In classical beam theory of damped vibrations, the damped resonance frequency is lower than the undamped natural frequency [40] which contradicts the measured effect. Although the general mechanisms of this effect still need to be investigated, a link between increasing particle damping and increasing

resonance frequency with increasing excitation amplitude seems conceivable. In addition, an explanation is still to be found why the resonance frequencies of the cavity specimens in the fourth bending mode are lower than the resonance frequencies of the solid specimens.

As mentioned, the movement of powder is necessary to dissipate energy via the described mechanisms. Of special interest is, therefore, the ability of the powder to move, which is assumed to be reduced when the powder is packed more densely. The CT scans in Fig. 12 show areas with higher packing density after shaking, which shows a settling of the powder during shaking in the direction of gravity $\vec{g}_{\text{shake}}$. This seems to be the root cause for the decrease of loss factor over shaking duration, see Fig. 11. It is additionally assumed that the settled powder gets into a mesostable state, as the powder does not reorientate inside of the cavity in the direction of gravity during CT scanning $\vec{g}_{\text{CT}}$. This conclusion is drawn from the fact that there is no gradient of packing density in the direction of gravity during CT scanning $\vec{g}_{\text{CT}}$ or formation of empty space at the cavity side against this direction. It is, therefore, deduced that the particles in the present study could have a lower tendency to move in the cavity compared to previous studies, which showed empty spaces existing extensively in bigger cavities [25, 28, 30] or with powders of smaller particle size [38]. As the specimens in the present study have comparably small cavities filled with coarser powder, a lower tendency to move is assumed which causes the decrease in loss factor. An explanation is still to be found, why the decrease in loss factor is mainly seen in the third and fourth bending mode. The correlation between the decrease in loss factor and the total damping effect of the specific specimen could also be based on the specimen-dependent movability of the powder in the cavity. Specimen #2 experiences a significantly lower damping effect but its loss factor does not decrease as much as specimen #1 and #3, compare Figs. 10, 11. One possible explanation is that the powder in the cavity of specimen #2 is denser packed prior to the experiment due to possible non-regular specimen handling. During shaking, the powder could, therefore, just settle slightly and loose only some of its damping abilities. Another possible explanation is the position of specimen #2 on the build plate during manufacturing between the other specimens, see Fig. 3. This could have resulted in a higher exposure to spatter or heat from the two adjacent specimens, which could have influenced the movability of the powder in the cavity. These hypotheses would need to be tackled with a study on the manufacturing parameter, especially the position and distance to other specimens on the build plate. Special care on specimen handling as well as shaking duration and amplitude would have to be taken care of. That is why only a qualitative analysis of the decrease in loss factor over shaking duration is conducted in the present study, as there are unmeasured times on the shaker due to the experimental procedure, see Fig. 11. Therefore, an additional, unmeasured decrease in loss factor is probable. This makes the settling effect even more significant and opens room for scientific studies to analyse the effect based on at least two parameters: At first, the long-term behaviour due to a constant force (like gravity) at different excitation amplitudes has to be investigated. Second, the external force could be increased to simulate other external forces like the centrifugal force, which is relevant in, e.g., turbine applications. In addition, measures to reactive the damping effect in specimens with densely packed powder have to be analysed.

5 Conclusion

The present study contributes to a better understanding of the governing influencing factors of AM particle damping with thin and flat cavities. It is shown that a damping effect of up to 564% can be achieved for AlSi10Mg specimens. However, this damping effect is dependent on the mode, excitation amplitude and even specific specimen. The highest damping is found in the third bending mode at the highest excited amplitude of 800 mm/s^2 in case of specimen #1. The two key findings of the present study are (1) the dependency of the damping effect on the specific cavity specimen and (2) the significant settling effect of the powder in the cavity which can be identified in CT scans and has an unfavourable effect on the damping characteristics over shaking duration. This settling effect has the potential to be subject of further scientific studies as well as relevant for future industrial applications.

Acknowledgements We thank the Institute of Design and Production Technology at the University of the Bundeswehr Munich for manufacturing the specimens. We also thank Dr.-Ing. Bruno Musil and Dr.-Ing. Pablo Vitale for comments on the manuscript. This research paper is funded by dtec.bw – Digitalization and Technology Research Center of the Bundeswehr which we gratefully acknowledge [project FLAB-3Dprint]. dtec.bw is funded by the European Union – NextGenerationEU.

Funding Open Access funding enabled and organized by Projekt DEAL. All authors certify that they have no affiliations with or involvement in any organization or entity with any financial interest or non-financial interest in the subject matter or materials discussed in this manuscript.

Data availability The data that support the findings of this study are openly available in Zenodo at https://doi.org/10.5281/zenodo.7760081.

References

1. Liu G, Zhang X, Chen X et al (2021) Additive manufacturing of structural materials. Mater Sci Eng: R: Rep. https://doi.org/10.1016/j.mser.2020.100596
2. May D (2021) Integrated Product Development with Fiber-Reinforced Polymers, 1st edn. Springer International Publishing, Cham, Engineering Materials
3. Stoll HW (1986) Design for manufacture: an overview. Appl Mech Rev 39:1356–1364. https://doi.org/10.1115/1.3149526
4. Degischer H-P, Lüftl S (2009) Leichtbau: Prinzipien, Werkstoffauswahl und Fertigungsvarianten, 1st edn. Wiley-VCH, Weinheim
5. Suresh S (2020) Topology Optimization for Additive Manufacturing Involving High-Cycle Fatigue. Licentiate Thesis, Linköping University
6. EOS GmbH (2018) Additive Manufacturing for the new A350 XWB. https://www.eos.info/01_parts-and-applications/case_studies_applications_parts/_case_studies_pdf/en_cases/cs_m_aerospace_sogeti_en.pdf. Accessed 16 Aug 2022
7. EOS GmbH (2018) Certified for Universal Success: Additive Manufacturing of Satellite Components. https://www.eos.info/01_parts-and-applications/case_studies_applications_parts/_case_studies_pdf/en_cases/cs_m_aerospace_ruag_en.pdf. Accessed 16 Aug 2022
8. SLM Solutions Group AG (2019) Monolithic Thrust Chamber: Case Study. Additive Design Optimization with CellCore GmbH. https://www.slm-solutions.com/fileadmin/Content/Case_Studies/CaseStudy_CellCore_ThrustChamber_web.pdf. Accessed 16 Aug 2022
9. EOS GmbH (2019) Future Ariane Propulsion Module: Simplified by Additive Manufacturing. https://www.eos.info/01_parts-and-applications/case_studies_applications_parts/_case_studies_pdf/en_cases/cs_m_aerospace_arianegroup_en.pdf. Accessed 16 Aug 2022
10. Anusci V (2018) Airbus Helicopters to begin 3D printing metal A350 components. https://www.3dprintingmedia.network/airbus-helicopters-a350/. Accessed 09 Nov 2021
11. Airbus SAS (2014) Printing the future: Airbus expands its applications of the revolutionary additive layer manufacturing process. https://www.aerocontact.com/en/aerospace-aviation-news/44590-printing-the-future-airbus-expands-its-applications-of-the-revolutionary-additive-layer-manufacturing-process. Accessed 16 Aug 2022
12. Airbus SAS (2017) First titanium 3D-printed part installed into serial production aircraft. https://www.airbus.com/en/newsroom/press-releases/2017-09-first-titanium-3d-printed-part-installed-into-serial-production. Accessed 16 Aug 2022
13. EOS GmbH (2017) Advanced Manufacturing Process by EOS Optimizes Satellite Technology. https://www.eos.info/01_parts-and-applications/case_studies_applications_parts/_case_studies_pdf/en_cases/cs_m_aerospace_airbus_en.pdf. Accessed 16 Aug 2022
14. Vajna S, Gerhard D, Wartzack S et al (2018) CAx für Ingenieure: Eine praxisbezogene Einführung, 3rd edn. Springer Vieweg Berlin, Heidelberg
15. Liedl S (2000) Bewegungen und Kräfte des Seilsystems und der Fahrzeuge von Seilschwebebahnen im Fahrbetrieb. utzverlag GmbH, München
16. Kolerus J, Becker E (2022) Condition Monitoring und Instandhaltungsmanagement, 1st edn. expert verlag GmbH, Tübingen
17. Ehlers T, Lachmayer R (2020) Einsatz additiv gefertigter Partikeldämpfer – eine Übersicht. In: Kaierle S, Rettschlag K, Lachmayer R (eds) Konstruktion für die Additive Fertigung 2019, 1st edn. Springer Vieweg, Berlin, Heidelberg
18. Dinkler D (2017) Einführung in die Strukturdynamik: Modelle und Anwendungen, 2nd edn. Springer Vieweg, Wiesbaden
19. Zeller P (2018) Körperschall. In: Zeller P (ed) Handbuch Fahrzeugakustik: Grundlagen, Auslegung, Berechnung, Versuch, 3rd edn. Springer Fachmedien, Wiesbaden, pp 223–250
20. Marhadi KS, Kinra VK (2005) Particle impact damping: effect of mass ratio, material, and shape. J Sound Vib 283:433–448. https://doi.org/10.1016/j.jsv.2004.04.013
21. Sánchez M, Pugnaloni LA (2011) Effective mass overshoot in single degree of freedom mechanical systems with a particle damper. J Sound Vib 330:5812–5819. https://doi.org/10.1016/j.jsv.2011.07.016
22. Ben Romdhane M, Bouhaddi N, Trigui M et al (2013) The loss factor experimental characterisation of the non-obstructive particles damping approach. Mech Syst Signal Process 38:585–600. https://doi.org/10.1016/j.ymssp.2013.02.006
23. Friend RD, Kinra VK (2000) Particle impact damping. J Sound Vib 233:93–118. https://doi.org/10.1006/jsvi.1999.2795
24. Hopkinson N, Hague R, Dickens PM (2005) Rapid Manufacturing: An Industrial Revolution for the Digital Age. John Wiley Sons Ltd, Chichester, UK
25. Ehlers T, Tatzko S, Wallaschek J et al (2021) Design of particle dampers for additive manufacturing. Addit Manuf 38:1–19. https://doi.org/10.1016/j.addma.2020.101752
26. Mao K, Wang MY, Xu Z et al (2004) Simulation and characterization of particle damping in transient vibrations. J Vib Acoust 126:202–211. https://doi.org/10.1115/1.1687401
27. Fowler BL, Flint EM, Olson SE (2001) Design methodology for particle damping. In: Inman DJ (ed) Smart Structures and Materials 2001: Damping and Isolation, 1st edn. SPIE, 186–197
28. Ehlers T, Lachmayer R (2022) Design of particle dampers for laser powder bed fusion. Appl Sci 12:2237. https://doi.org/10.3390/app12042237
29. Schmitz T, Betters E, West J (2020) Increased damping through captured powder in additive manufacturing. Manuf Lett 25:1–5. https://doi.org/10.1016/j.mfglet.2020.05.003
30. Schmitz T, Gomez M, Ray B et al (2020) Damping and mode shape modification for additively manufactured walls with captured powder. Precis Eng 66:110–124. https://doi.org/10.1016/j.precisioneng.2020.07.002
31. Gomez M, Corson G, Heikkenen E et al (2021) Biologically-inspired rib designs for captured powder damping in additive manufacturing. Manuf Lett 28:35–41. https://doi.org/10.1016/j.mfglet.2021.03.002
32. Künneke T, Zimmer D (2021) Konstruktionsregeln für additiv gefertigte Partikeldämpfer/design rules for additive manufactured particle dampers. Konstruktion. https://doi.org/10.37544/0720-5953-2021-11-12-72
33. Künneke T, Zimmer D (2017) Funktionsintegration additiv gefertigter Dämpfungsstrukturen bei Biegeschwingungen. In: Zipsner T, Schramm B, Richard HA (eds) Additive Fertigung von Bauteilen und Strukturen, 1st edn. Springer Fachmedien, Wiesbaden, pp 61–74
34. Scott-Emuakpor O, George T, Runyon B et al (2019) Sustainability study of inherent damping in additively manufactured nickel alloy. AIAA J 57:456–461. https://doi.org/10.2514/1.J057608

35. Scott-Emuakpor O, Beck J, Runyon B et al (2020) Validating a multifactor model for damping performance of additively manufactured components. AIAA J 58:5440–5447. https://doi.org/10.2514/1.J059608
36. Scott-Emuakpor O, George T, Runyon B et al (2020) Assessing additive manufacturing repeatability of inherently damped nickel alloy components. J Eng Gas Turbines Power 142:031011-1–31018. https://doi.org/10.1115/1.4044314
37. Scott-Emuakpor O, George T, Runyon B et al. (2018) Investigating Damping Performance of Laser Powder Bed Fused Components With Unique Internal Structures. In: Volume 7C: Structures and Dynamics, 1st edn. American Society of Mechanical Engineers, pp 1–10
38. Scott-Emuakpor O, George T, Runyon B et al (2018) Forced-Response Verification of the Inherent Damping in Additive Manufactured Specimens. In: Kramer S, Jordan JL, Jin H et al (eds) Mechanics of Additive and Advanced Manufacturing, vol 8, 1st edn. Springer International Publishing, Cham
39. Hollkamp JJ, Gordon RW (1998) Experiments with Particle Damping. In: Davis LP (ed) Smart Structures and Materials 1998: Passive Damping and Isolation, 1st edn. SPIE
40. Clough RW, Penzien J (1991) Dynamics of structures, 18th edn. McGraw-Hill, New York
41. SLM Solutions Group AG Al-Alloy AlSi10Mg: Material Data Sheet. https://www.slm-solutions.com/fileadmin/Content/Powder/MDS/MDS_Al-Alloy_AlSi10Mg_0520_EN.pdf. Accessed 18 Aug 2022
42. Ostermann F (2007) Anwendungstechnologie Aluminium, 2nd edn. VDI-Buch, Springer, Dordrecht
43. DIN German Institute for Standardization (2018) Additive manufacturing - General principles - Terminology 01.040.25; 25.030(DIN EN ISO/ASTM 52900:2018)
44. SLM Solutions Group AG Fe-Alloy 316L (1.4404): Material Data Sheet. https://www.slm-solutions.com/fileadmin/Content/Powder/MDS/MDS_Fe-Alloy_316L_0820_V0.91_EN_LS.pdf. Accessed 18 Aug 2022
45. SLM Solutions Group AG Ni-Alloy IN718 / 2.4668: Material Data Sheet. https://www.slm-solutions.com/fileadmin/Content/Powder/MDS/MDS_Ni-Alloy_IN718_0719_EN.pdf. Accessed 18 Aug 2022
46. Nöckel D (2022) Charakterisierung von recycelten Metallpulvern für das Laserstrahlschmelzen. Universität der Bundeswehr München, Bachelorarbeit
47. Lippert RB (2018) Restriktionsgerechtes Gestalten gewichtsoptimierter Strukturbauteile für das Selektive Laserstrahlschmelzen. Dissertation, Gottfried Wilhelm Leibniz Universität Hannover
48. ASTM International (2017) Standard Test Method for Measuring Vibration-Damping Properties of Materials 91.120.20(ASTM-E0756–05R17)
49. Babaei Gavan K, van der Drift EWJM, Venstra WJ et al (2009) Effect of undercut on the resonant behaviour of silicon nitride cantilevers. J Micromech Microeng 19:35003. https://doi.org/10.1088/0960-1317/19/3/035003
50. Ewins DJ (2000) Modal Testing: Theory, Practice And application, 2nd edn. Engineering Dynamics Series, vol 10. Research Studies Press, Baldock, Hertfordshire, England